The MillenniumTNG project: the galaxy population at $z \geq 8$

Rahul Kannan [,1,2★] Volker Springel [,3] Lars Hernquist,[1] Rüdiger Pakmor [,3] Ana Maria Delgado,[1] Boryana Hadzhiyska,[1] César Hernández-Aguayo [,3] Monica Barrera,[3] Fulvio Ferlito,[3] Sownak Bose [,4] Simon D. M. White [,3] Carlos Frenk,[4] Aaron Smith [1] and Enrico Garaldi [3]

[1]*Center for Astrophysics | Harvard & Smithsonian, 60 Garden Street, Cambridge, MA 02138, USA*
[2]*Department of Physics and Astronomy, York University, 4700 Keele Street, Toronto, Ontario MJ3 1P3, Canada*
[3]*Max-Planck Institute for Astrophysics, Karl-Schwarzschild-Str. 1, D-85741 Garching, Germany*
[4]*Institute for Computational Cosmology, Department of Physics, Durham University, South Road, Durham, DH1 3LE, UK*

ABSTRACT

The early release science results from *JWST* have yielded an unexpected abundance of high-redshift luminous galaxies that seems to be in tension with current theories of galaxy formation. However, it is currently difficult to draw definitive conclusions form these results as the sources have not yet been spectroscopically confirmed. It is in any case important to establish baseline predictions from current state-of-the-art galaxy formation models that can be compared and contrasted with these new measurements. In this work, we use the new large-volume ($L_{box} \sim 740$ cMpc) hydrodynamic simulation of the MillenniumTNG project, suitably scaled to match results from higher resolution – smaller volume simulations, to make predictions for the high-redshift ($z \gtrsim 8$) galaxy population and compare them to recent *JWST* observations. We show that the simulated galaxy population is broadly consistent with observations until $z \sim 10$. From $z \approx 10$–12, the observations indicate a preference for a galaxy population that is largely dust-free, but is still consistent with the simulations. Beyond $z \gtrsim 12$, however, our simulation results underpredict the abundance of luminous galaxies and their star-formation rates by almost an order of magnitude. This indicates either an incomplete understanding of the new *JWST* data or a need for more sophisticated galaxy formation models that account for additional physical processes such as Population III stars, variable stellar initial mass functions, or even deviations from the standard ΛCDM model. We emphasize that any new process invoked to explain this tension should only significantly influence the galaxy population beyond $z \gtrsim 10$, while leaving the successful galaxy formation predictions of the fiducial model intact below this redshift.

Key words: methods: numerical – galaxies: formation – galaxies: evolution – cosmology: early Universe.

1 INTRODUCTION

Until recently, the galaxy population beyond $z \gtrsim 8$ was essentially unexplored. *Hubble Space Telescope* (*HST*) observations have only been able to detect about 1000 galaxies at $z = 6$–8, and an even lower number at higher redshifts (Livermore, Finkelstein & Lotz 2017; Atek et al. 2018). Most of these galaxies do not have a spectroscopic confirmation and only a handful of objects have been observed with complementary facilities such as the Atacama Large millimetre Array (ALMA; Decarli et al. 2018; Hashimoto et al. 2018) and the *Spitzer Space Telescope* (see for example Stefanon et al. 2021). However, recent results from *JWST* are already revolutionizing our study of the processes of galaxy formation and evolution in the early Universe. The large mirror and infrared frequency coverage in principle allows for the detection of rest-frame optical emission of galaxies all the way to $z \sim 20$ (Kalirai 2018; Williams et al. 2018). In fact, there are already numerous detections of galaxies at $z \gtrsim 10$ (see for example

Furtak et al. 2022) and and less certain claims of galaxy candidates up to $z \sim 17$ (Donnan et al. 2023; Harikane et al. 2022a).

Intriguingly, the early science observations with the *JWST* show an abundance of high-redshift luminous galaxies (Castellano et al. 2022; Donnan et al. 2023; Finkelstein et al. 2022; Harikane et al. 2022a; Naidu et al. 2022a) that are in tension with extrapolated estimates from galaxy formation models that are tuned to match the properties of low-redshift galaxies (Behroozi et al. 2019, 2020). In fact, some works have found extremely massive galaxies with stellar masses $M_\star \sim 10^{11}$ M$_\odot$ at $z \gtrsim 10$ (Labbe et al. 2022; Rodighiero et al. 2023). Given the small survey volume, these galaxies seem to have stellar masses that are larger than the available baryonic reservoir of their host dark matter haloes (Boylan-Kolchin 2022; Lovell et al. 2023). Various explanations for this discrepancy have been proposed, including early dark energy models (Smith et al. 2022a), variable stellar initial mass functions (IMF; Steinhardt et al. 2022), higher than expected star-formation conversion efficiencies or a metal-free Population III stellar population that is extremely UV bright, skewing the mass-to-light ratios of these early galaxies (Inayoshi et al. 2022). However, it is difficult to draw definitive conclusions from these first results as the sources have not yet

★ E-mail: rahul.kannan@cfa.harvard.edu

been spectroscopically confirmed and the photometric candidates are based on reductions using preliminary calibrations. In fact, recent works have pointed out that the high photometric fluxes of these galaxy candidates can be explained by young and low-mass stellar populations, eliminating the need to invoke unrealistically high stellar mass galaxies at these redshifts (Endsley et al. 2022). We also note that there have been a few instances of the same source being detected at different redshifts by different groups (Donnan et al. 2023; Zavala et al. 2022). While improvements in the photometric and astrometric calibrations have led to improved redshift estimates for some of the galaxies (Finkelstein et al. 2022), there are still uncertainties due to the sensitivity of the measurement to different galaxy spectral energy distribution (SED) templates used for photometric fitting (Endsley et al. 2022) and an inability to properly differentiate between a low-redshift dusty starburst galaxy and a high-redshift source (see for example Naidu et al. 2022b). It is also important to note that these observations cover small fields ($\lesssim 100$ arcmin^2) that are subject to significant cosmic variance, especially at these high redshifts (Steinhardt, Jespersen & Linzer 2021).

To robustly assess the potential tension with theory, it is important to establish reliable baseline predictions from current state-of-the-art galaxy formation models, so that they can be used to compare with these recent and forthcoming observations. While quite a few works have endeavoured to model the galaxy population in the reionization epoch ($6 \lesssim z \lesssim 10$; Dayal et al. 2014; Gnedin 2014; Ni et al. 2022), only a few models have made predictions in the extreme high-redshift regime ($z \geq 10$). These include estimates from semi-numerical (Mason, Trenti & Treu 2015; Behroozi et al. 2020), semi-analytic (Yung et al. 2019), and simulation (Wilkins et al. 2022) frameworks. Although hydrodynamical simulations provide a greater understanding of the underlying physical processes that govern the properties of high-redshift galaxies, they are quite expensive which limits their ability to model a large representative volume of the Universe with high-resolution. This is especially important at high redshift, where the source density is so low that only the most massive overdensities have had time to collapse into haloes. This drawback can be overcome by either running large-volume simulations that only simulate the high-redshift Universe (Feng et al. 2016; Bird et al. 2022) or resimulate sub-regions in a large volume with higher resolution to build up a composite luminosity function at these high redshifts (Lovell et al. 2021).

In this paper, we utilise the new large-volume ($L_{box} = 738.12$ cMpc) hydrodynamical simulation of the MillenniumTNG (MTNG) project to make predictions for the high-redshift ($z \geq 8$) galaxy population. This large volume allows us to make predictions for the rare objects that exist at these high redshifts. The simulation uses the IllustrisTNG (Weinberger et al. 2017; Pillepich et al. 2018b) physics model which has been shown to produce a realistic representation of the galaxy population at low redshifts (Marinacci et al. 2018; Nelson et al. 2018; Pillepich et al. 2018a; Tacchella et al. 2019). We supplement the MTNG simulation with three higher-resolution, smaller-volume simulations that share the same underlying galaxy formation model and the AREPO code base (Springel 2010), namely TNG50 (Pillepich et al. 2019), THESAN[1] (Garaldi et al. 2022; Kannan et al. 2022a; Smith et al. 2022b), and TNG300 (Springel et al. 2018). Combining these simulations allows us to make predictions over a wide halo mass range ($8 \lesssim \log(M_{halo}[M_\odot]) \lesssim 12.5$). We show simulation predictions for the galaxy stellar mass function, UV

luminosity functions (UVLFs), star-formation main sequence, metal content of galaxies, and cosmic star-formation rate density (SFRD). We compare the results to recent observational estimates from *JWST* and outline potential reasons for the (mis)match.

This paper is one of several studies introducing the MillenniumTNG (MTNG) project which aside from the hydrodynamic simulation analysed here also includes a series of large dark matter-only simulations, including models with massive neutrinos as an additional hot dark matter component. The companion paper by Hernández-Aguayo et al. (2022) details the full simulation suite, corresponding data products, and quantifies basic matter and halo clustering statistics. Pakmor et al. (2022) focuses on the hydrodynamical full physics simulation of the MTNG project with special emphasis on the properties of galaxy clusters. Barrera et al. (2022) presents a novel version of the L-galaxies semi-analytic model of galaxy formation and its application to lightcone outputs of the MTNG simulations. Bose et al. (2022) presents a study of galaxy clustering based on colour-selected galaxy samples. Ferlito et al. (2022) presents studies of weak gravitational lensing both in the dark matter and full physics runs. Contreras et al. (2022) shows how the cosmological parameters of MTNG can be constrained based on galaxy clustering measurements. Hadzhiyska et al. (2022a,b) examines aspects of halo occupation distribution modelling and finally Delgado et al. (2022) studies intrinsic alignments and galaxy shapes. The present work is structured as follows. We introduce our methodology in Section 2, while the main results are presented in Section 3. We summarize and discuss our conclusions in Section 4.

2 METHODS

We use the large-volume full-physics MillenniumTNG (MTNG) hydrodynamic simulation to make predictions for the high-redshift galaxy population. The full simulation suite of MTNG consists of several full physics and dark matter only N-body simulations of various box sizes and resolutions (see Hernández-Aguayo et al. 2022). In this work, we use the largest full-physics simulation of the project, labelled MTNG740, which has a box size of 738.12 cMpc on a side, resolved by 4320^3 dark matter and gas particles each, setting the mass resolutions to 1.62×10^8 M$_\odot$ and 3.10×10^7 M$_\odot$ for dark matter and baryons, respectively. The softening length for dark matter and star particles is set to 3.7 ckpc while the softening length for the gas varies with the local cell size, constrained by a minimum of 0.37 ckpc. The simulation is performed using the moving mesh code AREPO (Springel 2010), which solves the hydrodynamic (HD) equations on an unstructured Voronoi grid constructed from a set of mesh generating points that are allowed to move along with the underlying gas flow. A quasi-Lagrangian solution to the fluid equations is obtained by solving the Riemann problem at the interfaces between moving mesh cells in the rest-frame of the interface. Gravity is solved with a Tree-PM approach that uses an oct-tree (Barnes & Hut 1986) algorithm to estimate the short range gravitational forces and a Particle Mesh method (Springel et al. 2021) to compute the long range ones.

The simulation uses the IllustrisTNG (Marinacci et al. 2018; Naiman et al. 2018; Nelson et al. 2018, 2019a; Pillepich et al. 2018b; Springel et al. 2018) galaxy formation model that has empirical prescriptions for processes occurring below the grid scale of the simulation, like star and black hole formation, and associated feedback. The model builds upon the previous Illustris galaxy formation model (Vogelsberger et al. 2013, 2014a,b) and has improved prescriptions for thermal and kinetic feedback from stars (Pillepich et al. 2018a) and radio mode feedback from active galactic

---

[1] THESAN uses AREPO-RT, which is the radiation hydrodynamic extension to AREPO, comprehensively described in Kannan et al. (2019).

Table 1. Main numerical parameters of the different hydrodynamical simulations used in this work.

Name	$L_{\rm box}$ [cMpc]	$N_{\rm particles}$	$m_{\rm DM}$ [M$_\odot$]	$m_{\rm gas}$ [M$_\odot$]	$\epsilon_{\rm DM}$ [ckpc]	$\epsilon_{\rm gas}^{\rm min}$ [ckpc]
MTNG740	738.12	2×4320^3	1.62×10^8	3.10×10^7	3.7	0.37
TNG300	302.63	2×2500^3	5.90×10^7	1.09×10^7	1.48	0.37
THESAN	95.50	2×2100^3	3.12×10^6	5.82×10^5	2.2	2.2
TNG50	51.67	2×2160^3	4.58×10^5	8.41×10^4	0.30	0.07

The columns from left to right list the simulation name, box size, total number of particles, mass of dark matter (DM) particles, target mass of gas cells, DM gravitational softening length, and minimum gas softening.

nuclei (AGN; Weinberger et al. 2017). The interstellar medium is modelled as a two-phase gas where cold clumps are embedded in a smooth, hot phase produced by supernova explosions (Springel & Hernquist 2003). Most importantly for our work, this model has been shown to quite successfully reproduce a variety of low-redshift observations, among others, the observed galactic color bimodality (Nelson et al. 2018), color-dependent spatial distribution and clustering of galaxies (Springel et al. 2018), galaxy stellar mass function, galaxy sizes (Genel et al. 2018; Pillepich et al. 2018b), metal distributions (Naiman et al. 2018), magnetic field strength and structure (Marinacci et al. 2018), star formation main sequence (Donnari et al. 2019) and resolved star formation (Nelson et al. 2021), and galaxy morphologies (Rodriguez-Gomez et al. 2019; Tacchella et al. 2019). Recently, it has also been used to run coupled galaxy formation and reionization simulations (THESAN) which made predictions for various reionization ($5 \lesssim z \lesssim 10$) observables like the UV luminosity functions, stellar mass functions and the cosmic star-formation rate density (Kannan et al. 2022a). They have also been used to study 21 cm power spectra (Kannan et al. 2022a) including an effective bias expansion in redshift space (Qin et al. 2022), IGM–galaxy connections including ionizing mean free path (Garaldi et al. 2022), Lyα emission and transmission statistics (Smith et al. 2022b; Xu et al. 2022), multitracer line intensity mapping (Kannan et al. 2022b), and galaxy ionizing escape fractions (Yeh et al. 2022).

2.1 Combining simulations and resolution corrections

While the MTNG740 hydrodynamical simulation has quite a large volume allowing us to make predictions for the rare objects at high-redshifts, its relatively low resolution does not allow for accurate predictions of low-mass galaxies. To overcome this issue we combine the results of MTNG with three other simulations that use the same underlying galaxy formation model, namely TNG50 (Pillepich et al. 2019), THESAN (Kannan et al. 2022a; Garaldi et al. 2022; Smith et al. 2022b), and TNG300 (Springel et al. 2018). These simulations differ from each other in mass and spatial resolution and boxsize, as outlined in Table 1. The resolution differences lead to moderately different predictions for the galaxy population with the higher-resolution simulations having slightly higher star-formation efficiencies, as shown in Pillepich et al. (2018b). Therefore, obtaining consistent predictions over a large mass range by combining the various simulations requires correcting for the different resolutions. In this work, we take the predictions of TNG50 as the baseline and correct THESAN, TNG300 and MTNG740 results to match TNG50. TNG50 is used as baseline because it is the highest resolution simulation in our suite. Moreover, it has been shown that for well resolved galaxies, the IllustrisTNG model provides convergent results, with the resolution corrections becoming progressively smaller (or even

vanishing) when the resolution is improved (Pillepich et al. 2019). This is seen clearly in the left-hand panel Fig. 1, which plots the stellar mass of the galaxy as a function of halo mass. While the low-resolution TNG300 (dashed green curve) and MTNG740 (dashed magenta curve) simulations have stellar masses that are on average about ∼0.3 dex lower than the TNG50 (dashed cyan curve) results, the THESAN (dashed blue curve) and TNG50 practically lie on top of each other despite the mass resolutions differing by about a factor of ≈7.

We apply a methodology similar to that outlined in Pillepich et al. (2018b) and Vogelsberger et al. (2020) to make these corrections. The impact of the resolution on the halo mass is very small (Jenkins et al. 2001), so it can be used as a stable reference quantity to make the relevant resolution corrections. For each simulation, we divide the galaxies into 50 logarithmically spaced bins with the halo masses ranging from $10^{7.5}$ to $10^{12.5}$ M$_\odot$. In each of these bins and for all simulations we calculate the median stellar masses, star-formation rates, stellar and gas metallicities, and UV magnitudes ($M_{\rm UV}$) at 1500 Å. For each simulation, we only consider the range with 100 per cent completeness, i.e. every halo in the particular mass range must contain at least one stellar particle.[2] This helps to ensure that only properties of well-resolved haloes are considered in this work.

Each simulation only covers a portion of the mass range due to the different box sizes and resolutions, with overlapping predictions only available for a relatively small range of masses. To overcome this obstacle the resolution corrections are made in a hierarchical manner; i.e. the corrections for a particular simulation are calculated with respect to the next higher-resolution imulation in the series. So the MTNG740 corrections are calculated by taking TNG300 results as the baseline, TNG300 uses THESAN, and THESAN uses TNG50. Thus, the total correction for a particular simulation is the sum of the corrections for all higher-resolution simulations. The individual corrections are determined by calculating the average difference between the values of the simulations in the overlapping halo mass range. We note that the average difference is calculated in log space for the stellar masses, SFRs, and metallicities (Z), while the UV magnitude corrections are calculated as is, because these are already proportional to the log of luminosity. The correction is then applied

---

[2]We note that this is different from assuming that every halo with one star particle is resolved. As shown in Yeh et al. (2022), this resolution constraint is quite stringent and the completeness factor only becomes unity in haloes that are an order of magnitude heavier than the nominal resolution limit of the simulation. This constraint ensures that the median quantities like the stellar-mass halo-mass relation, star forming main sequence, mass metallicity relation etc., are converged (in the sense that they follow the same relation as high mass galaxies if extended to low masses). Since we are mainly interested in the median relations, this resolution constraint works well for the purposes of this paper.
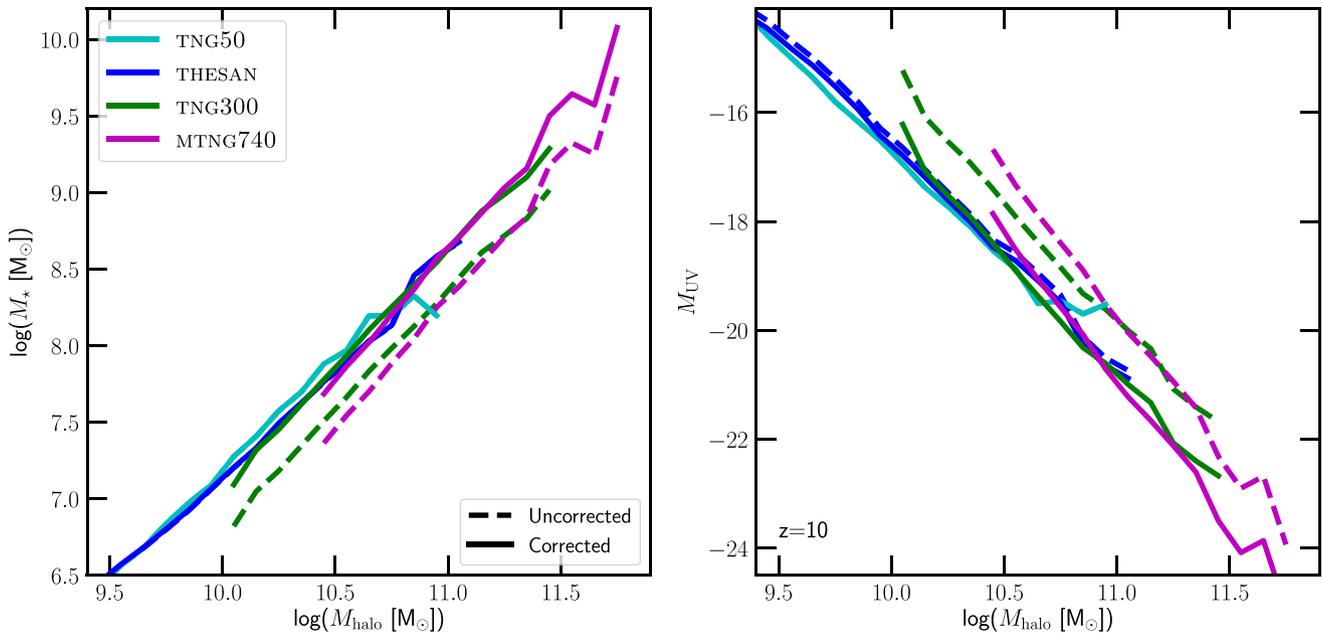
Figure 1. The stellar mass–halo mass (left-hand panel) and UV magnitude–halo mass (right-hand panel) relations for the TNG50 (cyan curves), THESAN (blue curves), TNG300 (green curves), and MTNG (magenta curves) simulations at $z = 10$. The dashed curves show intrinsic predictions while the solid lines are the results after correcting for the different resolutions of the simulations.

to all galaxies in the simulation, irrespective of whether they lie in the overlap region or not. This amounts to adding a constant calibration offset to all galaxies from lower-resolution simulations.

In Fig. 1, we show the outcome of this correction process on the predicted stellar mass–halo mass (left-hand panel) and M_{UV}–halo mass (right-hand panel) relations. The dashed curves show the uncorrected values for TNG50 (cyan curves), THESAN (blue curves), TNG300 (green curves), and MTNG740 (magenta curves), respectively, at $z = 10$, while the corresponding solid curves denote the corrected values. This approach of correcting for resolution in a hierarchical manner is well-suited for producing consistent predictions for a variety of quantities over a wide mass range. Finally, the corrected values of the different simulations are combined together to make a single forecast for the entire galaxy population. The stellar mass/luminosity functions are combined using $\Phi_{combined} = \Sigma(\Phi_i n_i^2)/(\Sigma n_i^2)$ where $i \in \{\text{TNG50, THESAN, TNG300, MTNG740}\}$, Φ is the mass/luminosity function, and n is the number of galaxies in the corresponding mass/luminosity bin (Vogelsberger et al. 2020). Other quantities Q (like the mean SFR) that do not rely on the number of galaxies within a certain bin are combined by using $Q_{combined} = \Sigma(Q_i n_i)/\Sigma(n_i)$.

3 RESULTS

In Fig. 2 we plot the stellar mass–halo mass (SMHM) relation at $z = 8$ (top left), $z = 9$ (top middle), $z = 10$ (top right), $z = 11$ (bottom left), $z = 12$ (bottom middle), and $z = 15$ (bottom right). The dashed curves show the resolution-corrected estimates for TNG50 (cyan curves), THESAN (blue curves), TNG300 (green curves), and MTNG740 (magenta curves), while the solid orange curves and corresponding shaded regions give the median and 1σ distribution of the simulated SMHM relation derived by combining all simulations using the method described in Section 2.1. For comparison, we

also include results from the abundance matching estimates from UNIVERSEMACHINE (black points; Behroozi et al. 2019). Our simulation results are in excellent agreement with these independent predictions, although the slopes of the relation are slightly different. The TNG model predicts slightly higher (lower) stellar masses at low (high) halo masses, with the discrepancy growing with increasing redshift. This provides further confidence that the procedures for resolution corrections and combining the different simulations used in this work are capable of providing reliable predictions over such a wide halo mass range.

Next, we turn our attention to Fig. 3, which plots the galaxy stellar mass function Φ (in units of cMpc^{-3} dex^{-1}) at $z = 8$–15, as indicated. The black solid curves show the simulation estimates while the orange curves are Schechter function fits (Schechter 1976), given by

$$\Phi \, d\log M = \ln(10) \, \Phi^* \frac{\left[10^{(\log M - \log M^*)}\right]^{\alpha+1}}{e^{10^{(\log M - \log M^*)}}} \, d\log M \,, \qquad (1)$$

where M is the stellar mass of the galaxy (in units of M$_\odot$), α is the low-mass slope, M^* is the stellar mass above which the mass function cuts off exponentially, and Φ^* is the value of the mass function at M^*. The values of these fits are listed in Table 2. The plot also shows observational estimates using lensed galaxy observations in the Hubble Frontier Fields from Bhatawdekar et al. (black crosses for disc-like source constraints and black pluses for point-like sources; 2019) and Kikuchihara et al. (black squares; 2020), *Spitzer*/IRAC measurements by Stefanon et al. (black circles; 2021)[3] and the recent gravitationally lensed galaxy candidates detected behind the galaxy cluster SMACS J0723.3-7327 (brown circle; Furtak et al. 2022). The

---

[3]The stellar mass estimates from Stefanon et al. (2021) have been converted to match the Chabrier IMF (Chabrier 2003) used in this work, reducing them by a factor of 1.7.
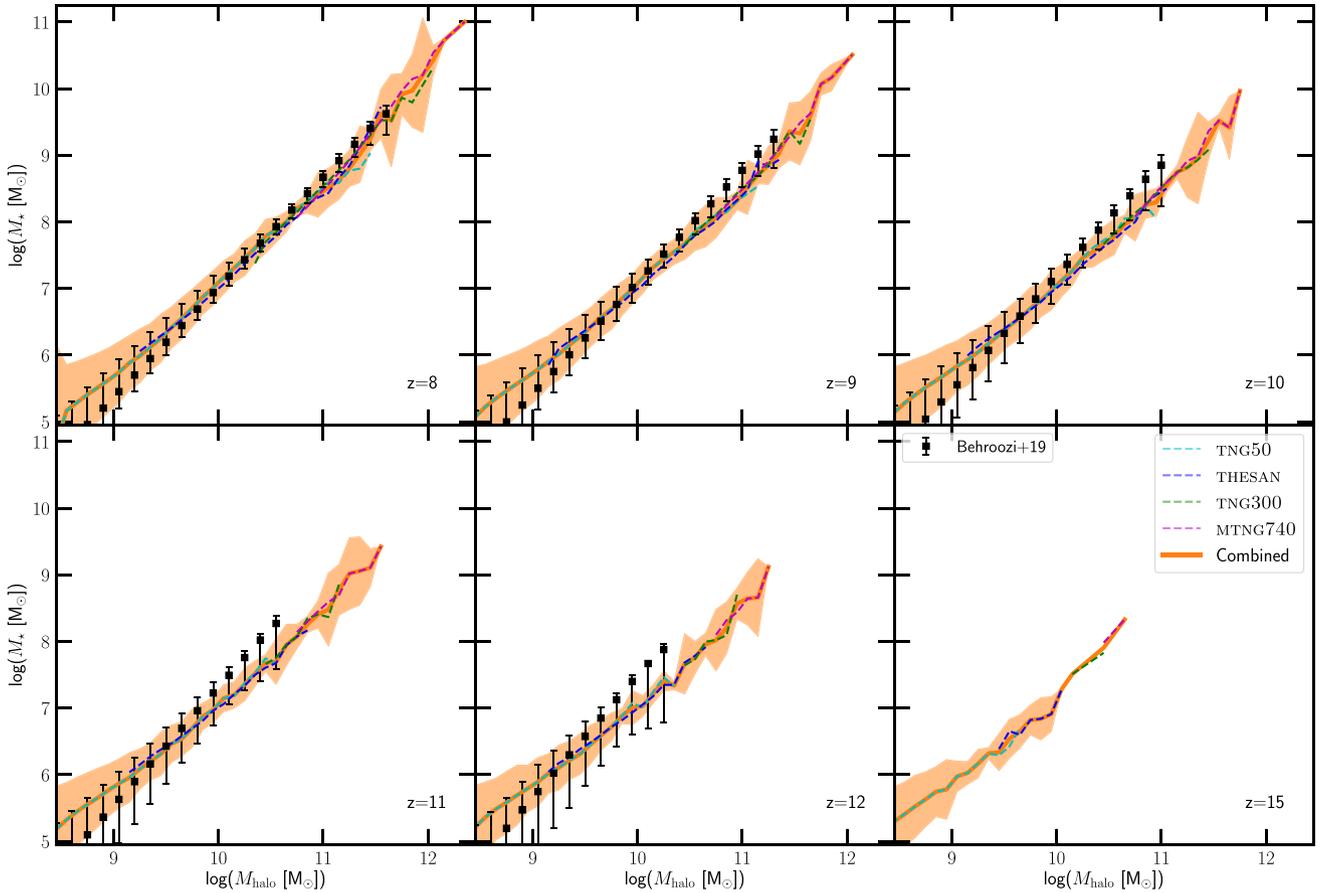
Figure 2. The stellar-halo mass relation at $z = 8$ (top left), $z = 9$ (top middle), $z = 10$ (top right), $z = 11$ (bottom left), $z = 12$ (bottom middle), and $z = 15$ (bottom right). The dashed curves show the relation for TNG50 (cyan curves), THESAN (blue curves), TNG300 (green curves) and MTNG740 (magenta curves), while the solid orange curves show the combined relation obtained with the methodology described in Section 2. The shaded region denotes the 1σ dispersion in the relation. The black points are the abundance matching estimates from UNIVERSEMACHINE (Behroozi et al. 2019). The simulations are broadly in agreement with the abundance matching results, but the TNG model seems to predict slightly lower star-formation efficiencies in high-mass haloes ($\log(M_{\rm halo}[{\rm M_\odot}]) \gtrsim 10.5$).

previous *HST/Spitzer* estimates are in general agreement with the simulation results up to $z \sim 10$ over a wide mass range. On the other hand, the new $z \sim 15$ *JWST* observations seem to indicate an overabundance of massive galaxies in the early Universe.

A more direct comparison with observations can be made by considering the UV luminosity function at $z = 8$–15, as shown in Fig. 4. For the TNG50, THESAN, and TNG300 simulations this is obtained by summing up the radiation output at rest-frame 1500 Å (using BPASS version 2.2.1 tables; Eldridge et al. 2017) of all the stars in the identified subhalo.[4] We note that due to the probabilistic nature of the star-formation routine, the star-formation history will only be sparsely sampled in haloes with low SFR. These haloes will have long periods with zero star formation interspersed with sudden jumps in SFR as a new particle is stochastically spawned. This young and massive star will then dominate the entire radiation output of the galaxy, especially if the mass of the galaxy is close to the

resolution limit of the simulation. This will adversely affect the UV luminosity function of the simulation. To overcome this numerical artefact, the age and mass of stars formed less than 5 Myr ago are smoothed over a timescale given by $t_{\rm smooth} = \Sigma M_\star (< 5\,{\rm Myr})/{\rm SFR}_{\rm gal}$, where ${\rm SFR}_{\rm gal}$ is the instantaneous SFR of the corresponding galaxy calculated by summing up all the SF probabilities of the cells on the EoS (see Springel & Hernquist 2003, for more details). This smoothing procedure is only done for haloes with $t_{\rm smooth} > 5$ Myr. We note that this only affects haloes close to the resolution limit and allows for a more faithful prediction of the simulated UV luminosity function (Kannan et al. 2022a).

This method requires a knowledge of the ages and metallicities of all stars in the halo. While this information is available in the full simulation snapshots, the MTNG740 simulation only outputs the SUBFIND and friends-of-friends halo catalogues at $z \gtrsim 7$. Therefore, it is not possible to derive the UV magnitudes at 1500 Å using raw particle/cell data. However, the group catalogue output includes the magnitudes in eight bands (U, B, V, K, g, r, i, z) based on the summed luminosities of all the stellar particles in each group (Torrey et al. 2015). These eight magnitudes are also derived from the distribution of stellar ages and metallicities, and therefore contain all the information needed to predict the value at 1500 Å as well. We exploit this by training a Ridge regression model on the eight band

---

[4]In this work we have not included nebular emission lines, which can in principle contribute significantly to the photometric fluxes, especially in high-redshift, low-metallicity environments. They have the ability to bias photometric estimates of the stellar mass and star formation rates (Endsley et al. 2022). However, there are very few strong emission lines around 1500 Å, so our theoretical estimates of $M_{\rm UV}$ should be quite robust.

Figure 3. The galaxy stellar mass function at $z = 8$–15 as labelled. The solid black curve gives the combined stellar mass function, while the orange curve depicts the Schechter function fit (equation 1; Schechter 1976) for the combined mass function, with the best-fitting parameters listed in Table 2. For comparison, we show results from *HST* and *Spitzer* observations by Bhatawdekar et al. (black crosses for disc-like source constraints and black pluses for point-like sources; 2019), Kikuchihara et al. (black squares; 2020), and Stefanon et al. (black circles; 2021), and recent *JWST* results from Furtak et al. (brown circles; 2022).

Table 2. Parameters for Schechter function fits of the galaxy stellar mass function at different redshifts (see equation 1).

z	α	$\log(M^*)$ [$\log(M_\odot)$]	$\log(\Phi^*)$ [cMpc^{-3} dex^{-1}]
8	-2.28 ± 0.02	10.68 ± 0.04	-6.60 ± 0.10
9	-2.42 ± 0.03	10.25 ± 0.08	-6.83 ± 0.19
10	-2.49 ± 0.06	9.66 ± 0.09	-6.51 ± 0.24
11	-2.49 ± 0.08	9.32 ± 0.10	-6.26 ± 0.29
12	-2.48 ± 0.13	8.71 ± 0.10	-5.74 ± 0.34
15	-2.56 ± 0.19	8.01 ± 0.12	-5.66 ± 0.43

outputs of the group catalogues to predict the 1500 Å magnitude using values from the TNG50, THESAN, and TNG300 simulations. This model is then employed to forecast M_{UV} at 1500 Å for galaxies in the MTNG740 simulation.

Attenuation by dust grains is especially important for the high-luminosity end. However, the amount of dust and its composition is not well constrained at these high redshifts. Therefore, we use an empirical dust-attenuation (A_{UV}) model, which is obtained by fitting the IRX–UV relationship inferred from ALMA observations at $z \sim$ 4–7 in Bouwens et al. (2016) to the following equation:

$$A_{UV} = 2.5 \log \left(1 + 10^{0.4\alpha_{dust}(M_{dust}(z) - M_{UV,int})} \right), \qquad (2)$$

where

$$M_{dust}(z) = M_{dust,0} + z \cdot M_{dust,z}, \qquad (3)$$

and the observed UV magnitude (M_{UV}) is $M_{UV,int} + A_{UV}$ (Behroozi et al. 2020). $M_{dust,z}$ is the magnitude below which the dust attenuation rises exponentially and it is a linear function of redshift (z) with $M_{dust,0}$ and $M_{dust,z}$ being the intercept and slope of the relation, respectively. Finally, α_{dust} is an opacity parameter that is roughly proportional to the optical depth at 1500 Å. We plot both the intrinsic (dashed black curves) and dust-attenuated (solid black curves) UV luminosity function, with the corresponding Schechter function fits for the intrinsic (dashed blue curves) and dust-attenuated UVLFs indicated by dashed blue and solid orange curves, respectively. The corresponding best-fitting parameters are given in Table 3. For comparison, we also plot the semi-empirical estimates from Behroozi et al.Behroozi et al. (purple curves; 2019) and post-processing dust radiative transfer calculations of TNG galaxies outlined in Vogelsberger et al. (2020). The results from Behroozi et al. (2019) are generally in good agreement with the dust-attenuated UVLFs, with only slight differences at $z = 15$. The Vogelsberger et al. (2020) results generally agree with ours, because we are looking at mostly the same galaxy population, only extended to higher luminosities due to the addition of the MTNG740 results. However, slight differences arise from the fact that the model for generating galactic SEDs is different between the two works. The pre-*JWST* estimates of the UVLF from Bouwens et al. (2015), Finkelstein et al.
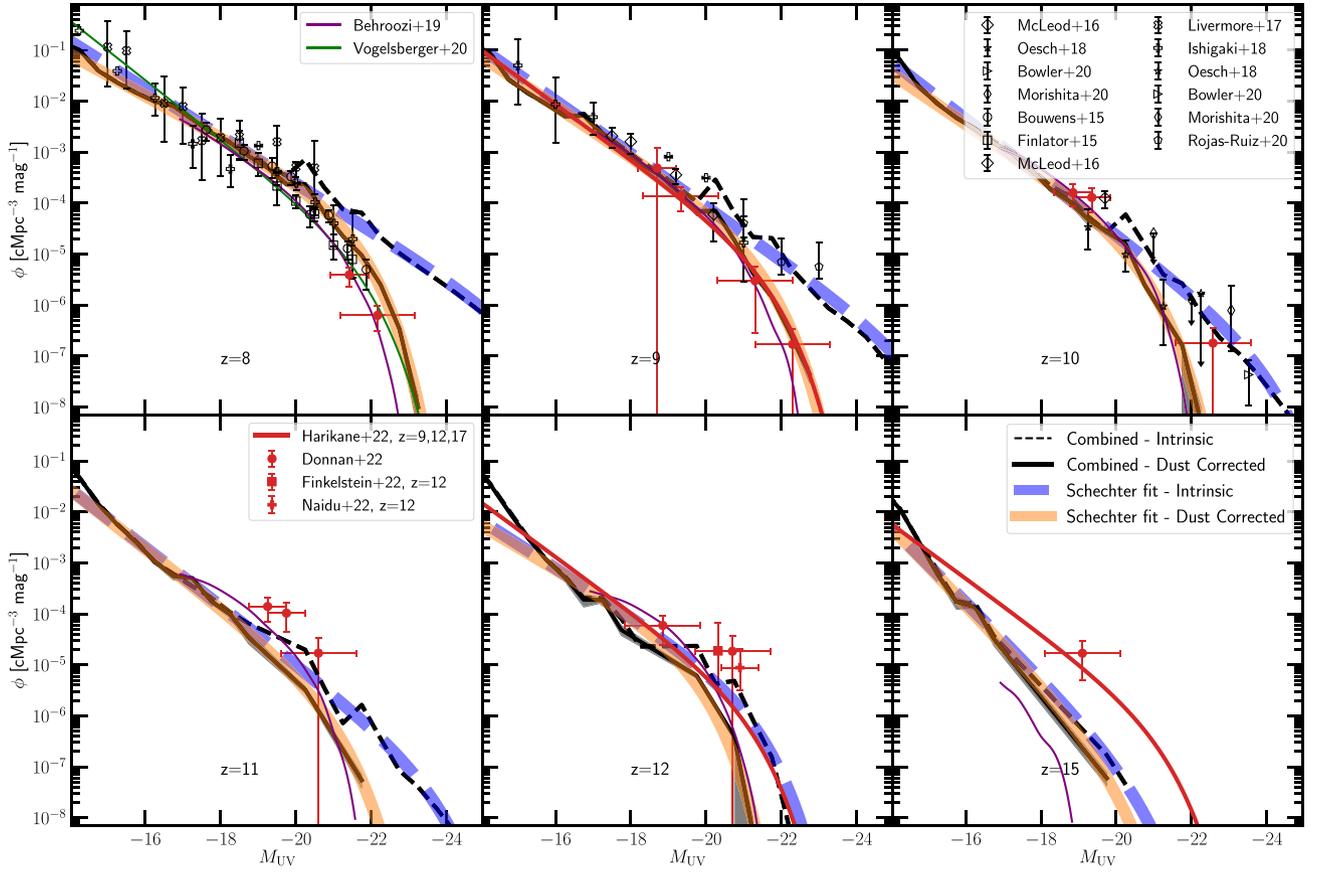
Figure 4. The UV luminosity function at $z = 8$–15 as labelled. The dashed black curves give the intrinsic UV luminosity function while the solid black curves show the dust-corrected values. The Schechter function fits for the intrinsic and dust-corrected UVLFs are shown as dashed blue and solid orange curves, respectively. For comparison, abundance matching estimates from Behroozi et al. (2019) are shown in purple, while the Schechter function fit to the estimates from the post-processing dust radiative transfer calculations by Vogelsberger et al. (2020) are shown in green. Pre-*JWST* measurements from Bouwens et al. (2015), Finkelstein et al. (2015), McLeod, McLure & Dunlop (2016), Livermore et al. (2017), Ishigaki et al. (2018), Oesch et al. (2018), Bowler et al. (2020), Morishita et al. (2020), and Rojas-Ruiz et al. (2020) are shown with black symbols as indicated. The new measurements from *JWST*, from Donnan et al. (2023), Finkelstein et al. (2022), and Naidu et al. (2022a), are plotted as filled red symbols, while the Schechter function fits to the observational estimates from Harikane et al. (2022a) are drawn as red curves.

Table 3. Schechter function fits for the galaxy luminosity functions.

z	α_{UV}	M^*_{UV} [mag]	$\log(\Phi^*_{UV})$ [cMpc^{-3} mag^{-1}]
8	-2.01 ± 0.03	-21.11 ± 0.04	-3.92 ± 0.06
9	-2.23 ± 0.05	-21.06 ± 0.10	-4.54 ± 0.12
10	-2.25 ± 0.05	-20.29 ± 0.07	-4.54 ± 0.11
11	-2.44 ± 0.06	-20.62 ± 0.14	-5.35 ± 0.17
12	-2.06 ± 0.27	-19.28 ± 0.27	-4.47 ± 0.41
15	-2.91 ± 0.39	-19.50 ± 1.26	-6.45 ± 1.52
		Intrinsic	
8	-2.16 ± 0.04	-26.07 ± 0.19	-6.40 ± 0.17
9	-2.30 ± 0.06	-25.36 ± 0.47	-6.83 ± 0.38
10	-2.42 ± 0.05	-23.69 ± 0.23	-6.68 ± 0.23
11	-2.43 ± 0.06	-23.34 ± 0.29	-6.87 ± 0.29
12	-2.18 ± 0.16	-20.90 ± 0.24	-5.39 ± 0.33
15	-2.84 ± 0.28	-20.28 ± 1.46	-6.89 ± 1.57

(2015), McLeod et al. (2016), Livermore et al. (2017), Ishigaki et al. (2018), Oesch et al. (2018), Bowler et al. (2020), Morishita et al. (2020), and Rojas-Ruiz et al. (2020) are presented as black unfilled symbols, as indicated. The recent *JWST* observational estimates from Donnan et al. (2023), Finkelstein et al. (2022), and Naidu et al. (2022a) are depicted as red filled symbols, while the Harikane et al. (2022a) Schechter function fits at $z = 9$, 12, and 17 are shown as red solid curves.

The dust-attenuated luminosity functions faithfully reproduce the observational estimates from both *HST* and *JWST* measurements at $z = 8$ and 9. At $z = 10$, however, there seems to be a higher than theoretically expected abundance of luminous ($M_{UV} < -22$) galaxies. In fact, the observations seem to prefer the dust-free UVLF, suggesting that most of the galaxies, even the brightest ones, are mainly dust free at these redshifts. At $z = 11$ and $z = 12$, the new *JWST* measurements seem to be slightly higher but still consistent with the simulated dust-free UVLF. This conclusion is supported by recent targeted ALMA observations of GHZ2/GLASS-z13, one of the brightest and most robust candidates at $z > 10$, by Bakx et al. (2022) who were unable to detect any dust continuum, indicating
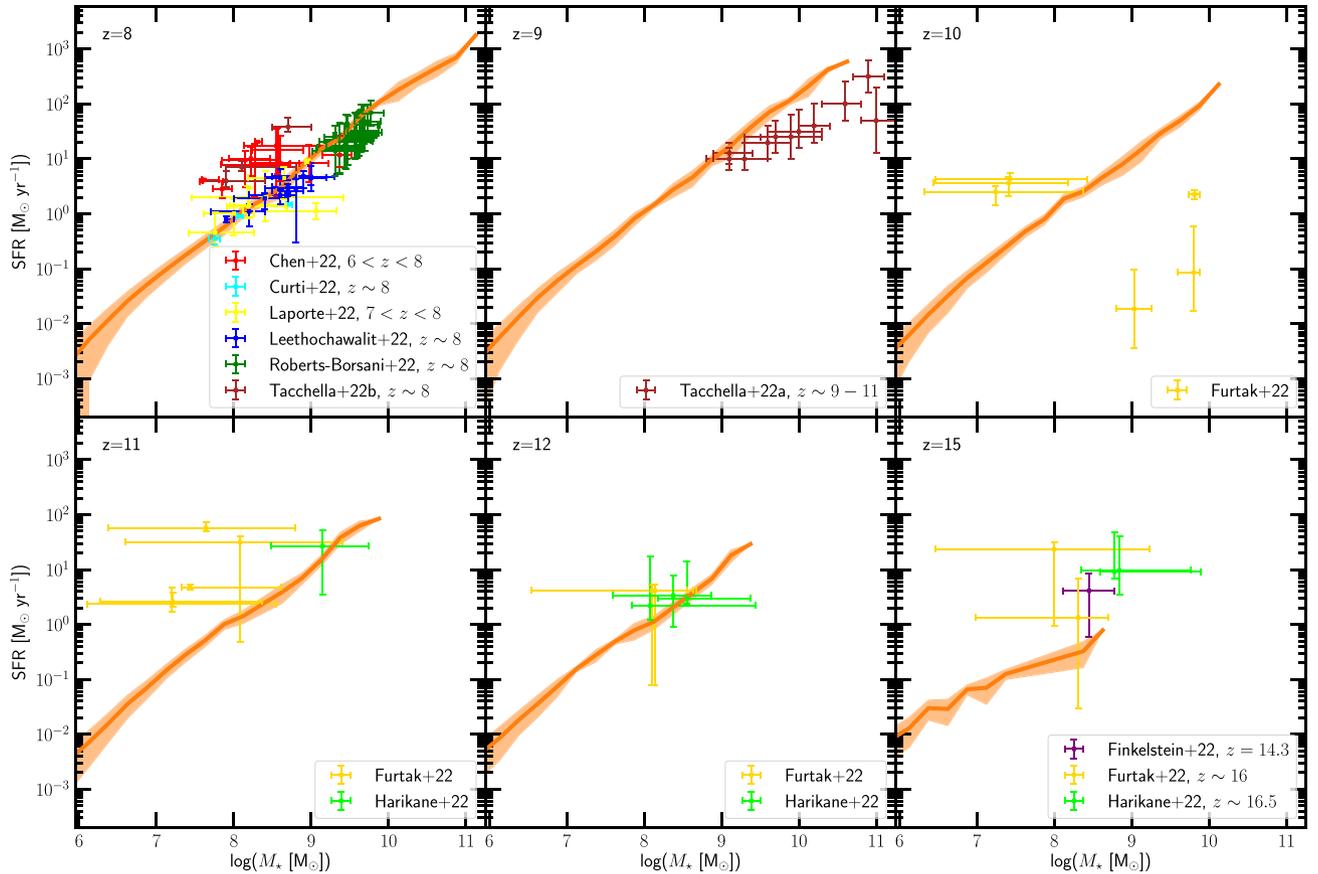
Figure 5. The predicted star-formation rate as a function of the stellar mass at $z = 8$–15 as labelled. The simulation results and their 1σ distributions are indicated by the orange curves and shaded regions, respectively. Observational estimates from Chen et al. (red points; 2023), Curti et al. (cyan points; 2023), Finkelstein et al. (purple points; 2022), Furtak et al. (gold points; 2022), Harikane et al. (light green points; 2022a), Laporte et al. (yellow points; 2022), Leethochawalit et al. (blue points; 2022), Roberts-Borsani et al. (dark green points; 2022), and Tacchella et al. (maroon points 2022a,b) are also shown for comparison.

negligible dust content in these high-redshift galaxies. However, by $z = 15$, the observed abundance of galaxies is about an order of magnitude higher than the simulated predictions.

These results seem to suggest that the star-formation and stellar feedback routines used in the TNG model, when combined with the adopted dust-attenuation estimates, do a good job of reproducing the galaxy population for $z \leq 10$. For $z = 10$–12, the observations seem to prefer a dust-free galaxy population (Ferrara, Pallottini & Dayal 2022), which is still consistent with the galaxy formation models that have been calibrated to match local Universe observations. However, the $z = 15$ discrepancy seems to suggest, at least when taken at face value, that we need to reexamine high-redshift galaxy formation physics and/or underlying cosmology. We will discuss this further in Section 4.

Additional insights into the reasons for this discrepancy can be inferred by inspecting the star-formation rate–stellar mass relation, also known as the star-formation main sequence (Whitaker et al. 2014). While the UVLF and GSMF can be biased by factors like cosmic variance (Steinhardt et al. 2021), the star-formation rate as a function of stellar mass is largely independent of the environment of galaxies and is therefore an excellent probe for the efficiency with which galaxies form stars. Fig. 5 shows the simulated (orange curves) star-formation main sequence at $z = 8$–15. A collection of observational estimates from a combination of *HST*, *Spitzer*/IRAC, and *JWST* observations presented in Chen et al.

(2023), Curti et al. (2023), Finkelstein et al. (2022), Furtak et al. (2022), Harikane et al. (2022a), Laporte et al. (2022), Leethochawalit et al. (2022), Roberts-Borsani et al. (2022), and Tacchella et al. (2022a,b) is shown as indicated. There is generally good agreement between the simulations and observational points, at least up to $z \simeq 12$, even with the recent *JWST* results. Only the SFRs of the gravitationally lensed galaxies detected behind the galaxy cluster SMACS J0723.3-7327 from Furtak et al. (2022) seem inconsistent. They estimate SFRs that are about 1–2 orders of magnitude above the simulated main sequence at the low-mass end ($M_\star < 10^8\,M_\odot$), while the SFRs of high-mass galaxies ($M_\star > 10^9\,M_\odot$) are below the main sequence by a similar amount. However, we do note that the stellar mass measurements have very large uncertainties due to the complexities of creating an accurate lensing model (see for example Atek et al. 2018). Above $z > 12$ however, almost all the observational measurements predict systematically higher SFRs by about a factor of $\sim$10, indicating missing physical processes that are not currently modelled in most simulation frameworks.

In a similar vein, the metal content of both the stellar and gaseous components of galaxies helps to constrain important physical processes that govern star formation and feedback, e.g. the amount of fuel available for star formation, where stars are formed, how metal enrichment by stars proceeds, and the role that outflows play in ejecting both mass and metals from galaxies (Tremonti et al. 2004). Stellar metallicity also influences the UV luminosity of stars, with
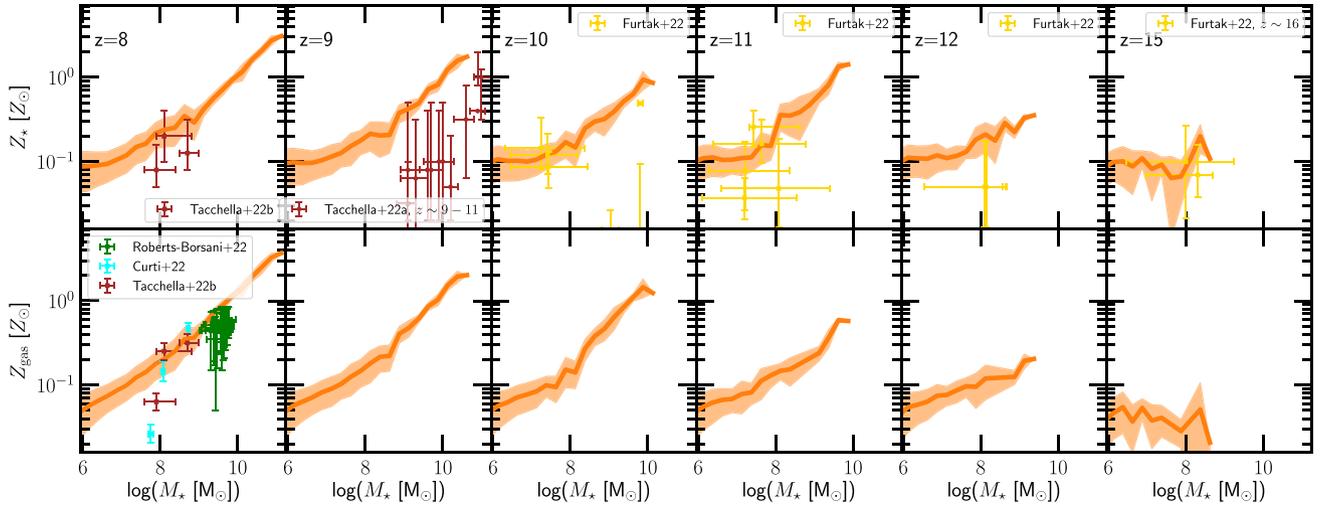
Figure 6. The predicted stellar (top rows) and gas phase (bottom rows) metallicity as a function of the stellar mass at $z = 8$–15 as labelled. The plot also includes observational estimates from Curti et al. (cyan points; 2023), Furtak et al. (gold points; 2022), Roberts-Borsani et al. (dark green points; 2022), and Tacchella et al. (maroon points 2022a,b).

low-metallicity stars emitting a larger number of high-energy photons (Eldridge et al. 2017). Moreover, increased metallicity can also lead to larger radiative cooling rates, which in turn provide more fuel for star formation (Wiersma, Schaye & Smith 2009). The average metallicity within galaxies is known to have a tight correlation with stellar mass, with low-mass galaxies being less metal enriched than the high-mass ones (Kewley & Ellison 2008).

In Fig. 6 we therefore plot the mass-weighted stellar (top panels) and gas phase (bottom panels) metallicity (scaled to the solar metallicity value $Z_\odot = 0.0127$) of galaxies as a function of their stellar mass. As expected, there is generally a positive correlation between the metallicity and stellar mass, however, the slope of this relation becomes shallower with increasing redshift. We note that this is in disagreement with previous work which found a very weak evolution of the slope of the mass–metallicity relation in the TNG model at $z = 2$–10 (Torrey et al. 2019). This might be due to the fact that these early galaxies are so young that there has not been enough time to establish a mass–metallicity relation. Even a single enrichment event can potentially increase the metallicity of low-mass galaxies to the levels seen in the high-mass ones. As expected the stellar metallicities are higher than gas phase ones, because the stars preferentially form in high-density gas that tends to be found in the metal enriched centres of galaxies. Interestingly, the observational estimates from Curti et al. (2023), Furtak et al. (2022), Roberts-Borsani et al. (2022), and Tacchella et al. (2022a,b) mainly derived from SED modelling of NIRCam photometry, are in good agreement with the simulated results even at $z = 15$. The fact that even the low-mass galaxies with very high SFRs, presented in Furtak et al. (2022), lie on the simulated mass–metallicity relation seems to imply that these galaxies are very young and are undergoing a massive starburst. However, we emphasize the high-mass galaxies that have very low SFRs are consistent with having hardly any metal enrichment at all ($< 0.01\,Z_\odot$). From a theory standpoint it is quite difficult to explain how these galaxies got quite so massive without enriching their gaseous and stellar components.

Finally, we turn our attention to the cosmic star-formation rate density as a function of redshift (Fig. 7), which is derived by integrating the Schechter function fits of the dust-free galaxy luminosity function (Table 3) down to $M_{\rm uv} = -17$, and converting the UV
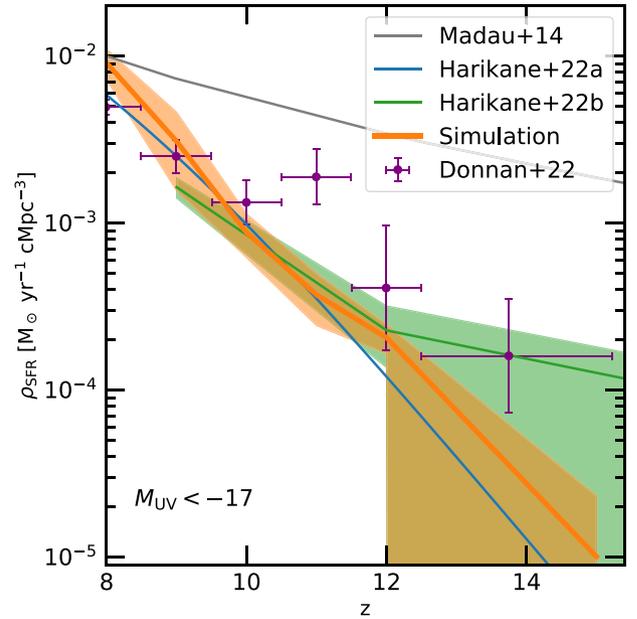
Figure 7. The cosmic SFRD for galaxies with $M_{\rm UV} < -17$. The simulation estimates (orange curve and shaded region) are calculated by using the Schechter function fits to the dust-free UVLF, and assuming a constant UV luminosity to star-formation rate ratio given by equation (4). The extrapolation from low-redshift fits from Madau & Dickinson (2014) is shown as the grey line. The green curve gives the estimate from Harikane et al. (2022a) using the Schechter function fits outlined in their paper. Finally, the purple points display the estimates from Donnan et al. (2023).

luminosity to a SFR using the relation

$$\text{SFR}\,[\text{M}_\odot\,\text{yr}^{-1}] = \kappa_{\rm UV} L_{\rm UV}\,[\text{erg}\,\text{s}^{-1}\,\text{Hz}^{-1}]\,, \qquad (4)$$

where $\kappa_{\rm UV}$ is a conversion factor that depends on the recent star-formation history, metal enrichment history, and initial mass function. To be consistent with the observational estimates we use $\kappa_{\rm UV} = 1.15 \times 10^{-28}\,\text{M}_\odot\,\text{yr}^{-1}/(\text{erg}\,\text{s}^{-1}\,\text{Hz}^{-1})$, which is valid for a Salpeter (1955) IMF and consistent with the cosmic star-formation

history out to $z \sim 8$ (Madau & Dickinson 2014). The plot also shows the SFR density estimates from the best-fitting function at $z \lesssim 8$ determined by Madau & Dickinson (grey curve; 2014) extrapolated beyond $z > 8$, and the estimates from Harikane et al. (2022a) which were derived assuming a constant star-formation efficiency. The newly derived observational estimates from *JWST* observations reported in Donnan et al. (purple points; 2023) and Harikane et al. (green curve; 2022b)[5] for the very first time put constraints on the star-formation rate beyond $z > 10$. The larger number of observed luminous galaxies at $z \gtrsim 13$ and the generally higher star-formation rates lead to a cosmic star-formation rate density that is about a factor of 2–5 higher than the simulation results. However, the simulation predictions are fairly consistent with the *JWST* observations at lower redshifts ($z \lesssim 12$). We therefore conclude that the simulations produce a realistic galaxy population below $z \leq 12$ but there might be some important physical processes missing at even higher redshifts.

4 DISCUSSION AND CONCLUSIONS

In this work we have presented a variety of predictions for the high-redshift ($z \geq 8$) galaxy population from the new MillenniumTNG (MTNG740) hydrodynamical simulation. In order to obtain consistent predictions over a wide halo ($8 \lesssim \log(M_{halo}[M_\odot]) \lesssim 12.5$) and stellar ($5 \lesssim \log(M_\star[M_\odot]) \lesssim 11$) mass range, we combine the results of MTNG740 with TNG50 (Nelson et al. 2019b; Pillepich et al. 2019), THESAN (Garaldi et al. 2022; Kannan et al. 2022a; Smith et al. 2022b), and TNG300 (Marinacci et al. 2018; Naiman et al. 2018; Nelson et al. 2018; Pillepich et al. 2018b; Springel et al. 2018), which all use the same underlying galaxy formation model. The different resolutions of these simulations lead to moderately offset predictions for the galaxy population, with the higher-resolution simulations having slightly higher star-formation efficiencies. We correct for this using the calibration methodology outlined in Section 2.1, using TNG50 (the highest resolution simulation in this suite) as baseline.

We make predictions for a variety of high-redshift galaxy properties, including the stellar-halo mass relation, galaxy stellar mass function, UV luminosity function, star-formation main sequence, metal enrichment in both stellar and gas phases, and cosmic star-formation rate density. These are compared to the recent observational estimates from *JWST* to determine the validity of the galaxy formation model (which has been calibrated to match the galaxy population in the local Universe) in this high-redshift frontier. The main results and conclusions of this work are as follows:

(i) The stellar-halo mass relation matches estimates from the abundance matching results of the UNIVERSEMACHINE model (Behroozi et al. 2019).

(ii) The predicted galaxy stellar mass functions match the observed estimates up to $z \sim 10$, but are below the new *JWST* estimates at $z = 15$.

(iii) The simulated UV luminosity function is consistent with both the *HST* and *JWST* estimates at $z = 8$ and 9. At $z = 10$, the observations seem to prefer a galaxy population that is largely free of dust. The $z = 11$ and 12 dust-free luminosity functions are slightly lower but still consistent with the new *JWST* measurements. However, by $z = 15$, the observed abundance of luminous galaxies is about an order of magnitude higher than the simulated results. Similar

results have also been found by other galaxy formation models that have been successful in reproducing the properties of low-redshift galaxies (see for example Moster, Naab & White 2018; Yung et al. 2019; Behroozi et al. 2020; Wilkins et al. 2022) although the degree to which they disagree with the new observations is different across various models.

(iv) This behaviour is reflected in the star-formation main sequence and the cosmic star-formation rate density (for galaxies with $M_{UV} < -17$), with the simulated results generally being consistent with observational estimates below $z \lesssim 12$, but being lower by about an order of magnitude at $z = 15$.

(v) The metal content in galaxies seems to be consistent with the observations, despite some of the observations showing higher than expected star-formation rates. This suggests that most of the observationally detected galaxies have very young ages with most of the stars in these galaxies being formed very recently (Furtak et al. 2022; Mason, Trenti & Treu 2022).

(vi) The abundance of massive luminous galaxies observed with *JWST* seems to suggest, at least at face value, a need to rethink the galaxy formation physics. For example, by appealing to high star-formation efficiencies of about 10–30 per cent at high redshifts compared to just a few per cent in the local Universe (Moster, Naab & White 2013), a metal-deficient Population III dominated stellar population that produces more intense UV radiation (Inayoshi et al. 2022), temperature-dependant IMF (Sneppen et al. 2022; Steinhardt et al. 2022), or different dark energy models (Boylan-Kolchin 2022; Menci et al. 2022; Smith et al. 2022a). Alternatively, due to the current lack of spectroscopic confirmations, it might simply point to yet unknown systematic uncertainties like selection effects (Mason et al. 2022), incorrect estimates of the redshift (Finkelstein et al. 2022), or disparate star-formation histories (Endsley et al. 2022; Tacchella et al. 2022b).

One issue that might affect the results presented in this work is the relatively low resolution of the largest-volume MTNG740 simulation. While we have tried to correct for this by scaling up the results to match the highest-resolution TNG50 simulation, this procedure will not fully resolve this problem because the formation of the very first galaxies is still delayed in the low-resolution runs. We hope to overcome this in the near future, by performing higher-resolution, large-volume simulations, but only running them down to $z = 10$, to keep the computational cost down. In conclusion, if the results of the early release *JWST* observations are spectroscopically confirmed then it might require more sophisticated galaxy formation modelling that takes into account additional physics that so far has not been broadly incorporated into most galaxy formation models. However, we note that any new process invoked to solve this tension must only affect the properties of galaxies at very high redshifts, such that by $z = 10$ and below the successful predictions of the fiducial galaxy formation model, which has been tuned to match local Universe observations, are not altered. It is not yet clear which physics modifications can fulfil this non-trivial constraint. We plan to investigate some of these interesting possibilities in future works.

---

[5]We note that the cosmic star-formation rate density attributed to Harikane et al. (2022b) is derived by using the Schechter function fits quoted in their paper, instead of the double power-law fits, in order to be consistent with the framework used in our current work.

DATA AVAILABILITY

The data underlying this article will be shared upon reasonable request to the corresponding authors. All MTNG simulations will be made publicly available in 2024 at www.mtng-project.org. All THESAN simulation data will be made publicly available in the near future and distributed via www.thesan-project.com.

REFERENCES

Atek H., Richard J., Kneib J.-P., Schaerer D., 2018, MNRAS, 479, 5184

Bakx T. J. L. C. et al., 2022, preprint (arXiv:2208.13642)

Barnes J., Hut P., 1986, Nature, 324, 446

Barrera M. et al., 2022, preprint (arXiv:2210.10419)

Behroozi P., Wechsler R. H., Hearin A. P., Conroy C., 2019, MNRAS, 488, 3143

Behroozi P. et al., 2020, MNRAS, 499, 5702

Bhatawdekar R., Conselice C. J., Margalef-Bentabol B., Duncan K., 2019, MNRAS, 486, 3805

Bird S., Ni Y., Di Matteo T., Croft R., Feng Y., Chen N., 2022, MNRAS, 512, 3703

Bose S. et al., 2022, preprint (arXiv:2210.10065)

Bouwens R. J. et al., 2015, ApJ, 803, 34

Bouwens R. J. et al., 2016, ApJ, 833, 72

Bowler R. A. A., Jarvis M. J., Dunlop J. S., McLure R. J., McLeod D. J., Adams N. J., Milvang-Jensen B., McCracken H. J., 2020, MNRAS, 493, 2059

Boylan-Kolchin M., 2022, preprint (arXiv:2208.01611)

Castellano M. et al., 2022, ApJL, 938, L15

Chabrier G., 2003, ApJ, 586, L133

Chen Z., Stark D. P., Endsley R., Topping M., Whitler L., Charlot S., 2023, MNRAS, 518, 5607

Contreras S. et al., 2022, preprint (arXiv:2210.10075)

Curti M. et al., 2023, MNRAS, 518, 425

Dayal P., Ferrara A., Dunlop J. S., Pacucci F., 2014, MNRAS, 445, 2545

Decarli R. et al., 2018, ApJ, 854, 97

Delgado A. M. et al., 2022, in preparation

Donnan C. T. et al., 2023, MNRAS, 518, 6011

Donnari M. et al., 2019, MNRAS, 485, 4817

Eldridge J. J., Stanway E. R., Xiao L., McClelland L. A. S., Taylor G., Ng M., Greis S. M. L., Bray J. C., 2017, PASA, 34, e058

Endsley R., Stark D. P., Whitler L., Topping M. W., Chen Z., Plat A., Chisholm J., Charlot S., 2022, preprint (arXiv:2208.14999)

Feng Y., Di-Matteo T., Croft R. A., Bird S., Battaglia N., Wilkins S., 2016, MNRAS, 455, 2778

Ferlito F. et al., 2022. in preparation

Ferrara A., Pallottini A., Dayal P., 2022, preprint (arXiv:2208.00720)

Finkelstein S. L. et al., 2015, ApJ, 810, 71

Finkelstein S. L. et al., 2022, ApJL, 940, L55

Furtak L. J., Shuntov M., Atek H., Zitrin A., Richard J., Lehnert M. D., Chevallard J., 2022, preprint (arXiv:2208.05473)

Garaldi E., Kannan R., Smith A., Springel V., Pakmor R., Vogelsberger M., Hernquist L., 2022, MNRAS, 512, 4909

Genel S. et al., 2018, MNRAS, 474, 3976

Gnedin N. Y., 2014, ApJ, 793, 29

Hadzhiyska B. et al., 2022a, preprint (arXiv:2210.10068)

Hadzhiyska B. et al., 2022b, preprint (arXiv:2210.10072)

Harikane Y. et al., 2022a, preprint (arXiv:2208.01612)

Harikane Y. et al., 2022b, ApJ, 929, 1

Hashimoto T. et al., 2018, Nature, 557, 392

Hernández-Aguayo C. et al., 2022, preprint (arXiv:2210.10059)

Inayoshi K., Harikane Y., Inoue A. K., Li W., Ho L. C., 2022, ApJL, 938, L10

Ishigaki M., Kawamata R., Ouchi M., Oguri M., Shimasaku K., Ono Y., 2018, ApJ, 854, 73

Jenkins A., Frenk C. S., White S. D. M., Colberg J. M., Cole S., Evrard A. E., Couchman H. M. P., Yoshida N., 2001, MNRAS, 321, 372

Kalirai J., 2018, Contemp. Phys., 59, 251

Kannan R., Vogelsberger M., Marinacci F., McKinnon R., Pakmor R., Springel V., 2019, MNRAS, 485, 117

Kannan R., Garaldi E., Smith A., Pakmor R., Springel V., Vogelsberger M., Hernquist L., 2022a, MNRAS, 511, 4005

Kannan R., Smith A., Garaldi E., Shen X., Vogelsberger M., Pakmor R., Springel V., Hernquist L., 2022b, MNRAS, 514, 3857

Kewley L. J., Ellison S. L., 2008, ApJ, 681, 1183

Kikuchihara S. et al., 2020, ApJ, 893, 60

Labbe I. et al., 2022, preprint (arXiv:2207.12446)

Laporte N., Zitrin A., Dole H., Roberts-Borsani G., Furtak L. J., Witten C., 2022, A&A, 667, L3

Leethochawalit N. et al., 2022, preprint (arXiv:2207.11135)

Livermore R. C., Finkelstein S. L., Lotz J. M., 2017, ApJ, 835, 113

Lovell C. C., Vijayan A. P., Thomas P. A., Wilkins S. M., Barnes D. J., Irodotou D., Roper W., 2021, MNRAS, 500, 2127

Lovell C. C., Harrison I., Harikane Y., Tacchella S., Wilkins S. M., 2023, MNRAS, 518, 2511

McLeod D. J., McLure R. J., Dunlop J. S., 2016, MNRAS, 459, 3812

Madau P., Dickinson M., 2014, ARA&A, 52, 415

Marinacci F. et al., 2018, MNRAS, 480, 5113

Mason C. A., Trenti M., Treu T., 2015, ApJ, 813, 21

Mason C. A., Trenti M., Treu T., 2022, preprint (arXiv:2207.14808)

Menci N., Castellano M., Santini P., Merlin E., Fontana A., Shankar F., 2022, ApJ, 938, L5

Morishita T. et al., 2020, ApJ, 904, 50

Moster B. P., Naab T., White S. D. M., 2013, MNRAS, 428, 3121

Moster B. P., Naab T., White S. D. M., 2018, MNRAS, 477, 1822

Naidu R. P. et al., 2022a, ApJL, 940, L14

Naidu R. P. et al., 2022b, preprint (arXiv:2208.02794)

Naiman J. P. et al., 2018, MNRAS, 477, 1206

Nelson D. et al., 2018, MNRAS, 475, 624

Nelson D. et al., 2019a, Comput. Astrophys. Cosmol., 6, 2

Nelson D. et al., 2019b, MNRAS, 490, 3234

Nelson E. J. et al., 2021, MNRAS, 508, 219

Ni Y. et al., 2022, MNRAS, 513, 670

Oesch P. A., Bouwens R. J., Illingworth G. D., Labbé I., Stefanon M., 2018, ApJ, 855, 105

Pakmor R. et al., 2022, preprint (arXiv:2210.10060)

Pillepich A. et al., 2018a, MNRAS, 473, 4077

Pillepich A. et al., 2018b, MNRAS, 475, 648

Pillepich A. et al., 2019, MNRAS, 490, 3196

Qin W., Schutz K., Smith A., Garaldi E., Kannan R., Slatyer T. R., Vogelsberger M., 2022, PRD, 106, 123506

Roberts-Borsani G., Morishita T., Treu T., Leethochawalit N., Trenti M., 2022, ApJ, 927, 236

Rodighiero G., Bisigello L., Iani E., Marasco A., Grazian A., Sinigaglia F., Cassata P., Gruppioni C., 2023, MNRAS, 518, L19

Rodriguez-Gomez V. et al., 2019, MNRAS, 483, 4140

Rojas-Ruiz S., Finkelstein S. L., Bagley M. B., Stevans M., Finkelstein K. D., Larson R., Mechtley M., Diekmann J., 2020, ApJ, 891, 146

Salpeter E. E., 1955, ApJ, 121, 161

Schechter P., 1976, ApJ, 203, 297

Smith T. L., Lucca M., Poulin V., Abellan G. F., Balkenhol L., Benabed K., Galli S., Murgia R., 2022a, PRD, 106, 043526

Smith A., Kannan R., Garaldi E., Vogelsberger M., Pakmor R., Springel V., Hernquist L., 2022b, MNRAS, 512, 3243

Sneppen A., Steinhardt C. L., Hensley H., Jermyn A. S., Mostafa B., Weaver J. R., 2022, ApJ, 931, 57

Springel V., 2010, MNRAS, 401, 791

Springel V., Hernquist L., 2003, MNRAS, 339, 289

Springel V. et al., 2018, MNRAS, 475, 676

Springel V., Pakmor R., Zier O., Reinecke M., 2021, MNRAS, 506, 2871

Stefanon M., Bouwens R. J., Labbé I., Illingworth G. D., Gonzalez V., Oesch P. A., 2021, ApJ, 922, 29

Steinhardt C. L., Jespersen C. K., Linzer N. B., 2021, ApJ, 923, 8

Steinhardt C. L., Kokorev V., Rusakov V., Garcia E., Sneppen A., 2022, preprint (arXiv:2208.07879)

Tacchella S. et al., 2019, MNRAS, 487, 5416

Tacchella S. et al., 2022a, preprint (arXiv:2208.03281)

Tacchella S. et al., 2022b, ApJ, 927, 170

Torrey P. et al., 2015, MNRAS, 447, 2753

Torrey P. et al., 2019, MNRAS, 484, 5587

Tremonti C. A. et al., 2004, ApJ, 613, 898

Vogelsberger M., Genel S., Sijacki D., Torrey P., Springel V., Hernquist L., 2013, MNRAS, 436, 3031

Vogelsberger M. et al., 2014a, MNRAS, 444, 1518

Vogelsberger M. et al., 2014b, Nature, 509, 177

Vogelsberger M. et al., 2020, MNRAS, 492, 5167

Weinberger R. et al., 2017, MNRAS, 465, 3291

Whitaker K. E. et al., 2014, ApJ, 795, 104

Wiersma R. P. C., Schaye J., Smith B. D., 2009, MNRAS, 393, 99

Wilkins S. M. et al., 2022, preprint (arXiv:2204.09431)

Williams C. C. et al., 2018, ApJS, 236, 33

Xu C. et al., 2022, preprint (arXiv:2210.16275)

Yeh J. Y. C. et al., 2022, preprint (arXiv:2205.02238)

Yung L. Y. A., Somerville R. S., Finkelstein S. L., Popping G., Davé R., 2019, MNRAS, 483, 2983

Zavala J. A. et al., 2022, preprint (arXiv:2208.01816)

This paper has been typeset from a TEX/LATEX file prepared by the author.